Mihelčič, M., Slemenik Perše, L., Šest, E., Jerman, I., Giuliani, C., Di Carlo, G., Lavorgna, M., Šurca, A. K.

Development of solvent- and water-borne fluoropolymer protective coatings for patina-free bronze discs.

Progress in Organic Coatings 125 (December 2018), 266-278

which has been published at ***https://doi.org/10.1016/j.porgcoat.2018.09.014***

Development of solvent- and water-borne fluoropolymer protective coatings for patina-free bronze discs

Mohor Mihelčič[1], Lidija Slemenik Perše[1], Ervin Šest[1], Ivan Jerman[1], Chiara Giuliani[2], Gabriella Di Carlo[2], Marino Lavorgna[3], Angelja Kjara Surca*

[1] *National Institute of Chemistry, Hajdrihova 19, SI-1000 Ljubljana*

[2] *Institute for the Study of Nanostructured Materials, National Research Council (ISMN-CNR), Via Salaria km 29,300, 00015 Monterotondo (RM), Italy*

[3] *Institute for Polymers, Composites and Biomaterials, National Research Council of Italy (IPCB-CNR), P.le E. Fermi 1, 80055 Portici, Italy*

** Corresponding author: E-mail angelja.k.surca@ki.si; phone 00386-1-4760-254; fax: 00386-1-4760-300*

Abstract

Solvent- (SB) and water-borne (WB) fluoropolymer coatings were produced for the outdoor protection of bronze. The coatings were prepared from commercially available resins with alternating fluoroethylene/vinylether copolymers. Because any application of protective coatings on works of art requires that they be removable in accordance with conservation ethics, various approaches to achieve removability of coatings were tested. The influence of modifications was verified through comparisons of hydrophobic, compact and irremovable protective coatings. Consequently, we prepared four types of coatings: two SB coatings and two WB coatings. The first SB coating was designed to have a hydrophobic compact structure (SB-c coating), and the second SB coating was modified with the addition of agents that impart strippability (SB-h coating). The same approach was used for the preparation of the two WB coatings: a compact (WB-c) coating vs. a hydrophilic (WB-h) coating, the latter being prepared through the addition of hydrophilic polyisocyanate.

The surface properties of the coatings were compared using scanning electron (SEM) and atomic force (AFM) microscopy. WB coatings were found to be more homogeneous in comparison with SB coatings and to have lower surface roughness. Contact angles confirmed the more hydrophobic nature of SB coatings. Potentiodynamic polarisation measurements and accelerated corrosion tests (exposure to acid vapours) revealed that protection efficiency not only increased with thickness but significantly depended on the coating structure. The

structure of coatings depended on the rheological parameters of the formulations simulating their behaviour during storage, deposition, and formation of the dry coating. Combined electrochemical and vibrational spectroscopic experiments were used to simulate long-term outdoor exposure of the protective coatings. *Ex situ* IR RA spectroelectrochemical measurements showed that hydration was more prevalent with WB coatings, and oxidation of bronze at the interface eventually occurred (656 cm^{-1} band). WB coatings with more free C=O groups were more prone to degradation. *In situ* Raman spectroelectrochemistry confirmed the better protection efficiency of SB over WB coatings. The optical properties of the coatings on glass showed higher transmittance for WB coatings compared to SB coatings.

Keywords: bronze, fluoropolymer, protective coating, infrared spectroscopy, Raman spectroscopy, rheology

1. Introduction

One approach to achieve corrosion resistance for bronze works of art in outdoor environments is the use of protective coatings. The natural protective layer of patina that evolves during the exposure of bronze to air can protect the bronze [1]. Consequently, it is not surprising that patinas are also produced by artists for protective and colour effects [1,2]. However, in urban and industrial environments, the species in naturally formed patina may contribute to various corrosion processes [1]. For this reason, protective coatings can also be deposited directly on the bronze surface. The preparative aspect (i) of this study is oriented towards the development of fluoropolymer protective coatings for patina-free bronze while considering the removability requirements of conservators (Fig. 1A). The preparative approaches were tested on solvent-borne (SB) and water-borne (WB) coatings. The second aim (ii) is the use of advanced analytical approaches that combine electrochemical techniques with spectroscopy (IR, Raman) to obtain insight into the degradation mechanisms of the coatings (Fig. 1B).

(i) Preparative aspect. Although waxes and Incralac™ are currently the most used artificial protection of bronze objects, research into other possible protections remains active. Reports range from the use of organic protective films with inhibiting properties [3,4] and chitosan [5] to various coatings made via sol-gel [6] or prepared from formulations of polymeric resins

(methyl methacrylate [7], polyurethanes [8] and fluoropolymers based on polyvinylidene fluoride (PVDF) [4]).

PVDF coatings have been studied because they are known for their outstanding exterior durability and chemical and moisture resistance. Although fluorocarbons and hydrocarbons have different properties and express phase separation behaviour in some mixtures [9], the direct bonding of -CH_2-CF_2- units to PVDF enables the formation of a semicrystalline polymer with an extended zigzag chain. When PVDF is used for the protection of bronze, the dispersion of pigments and adhesion is not sufficient [4]. Consequently, physical mixing with acrylic modifiers was attempted, but adhesion only increased from poor to average [4]. Another possible strategy is the introduction of acrylic moieties in the polymerisation stage of polymer production, which significantly improves the properties in SB and WB formulations [10]. A similar approach, mixing various building blocks in the polymerisation process, was used for the production of fluoroethylene/vinyl ether (FEVE) alternating copolymers by AGC (Asahi Glass Company), Japan (Lumiflon products) [11]. Instead of -CH_2-CF_2- building units of PVDF, in which two incompatible moieties are linked by a covalent bond, the fluoroethylene monomer in FEVE is composed of -CF_2-CFX-. A certain amount of covalently bonded chlorine is present in FEVE structures, but despite this limitation, highly protective coatings have been produced, even for extreme situations (e.g., bridges) [11]. The solubility of FEVE is afforded by the regularly repeating vinylether pattern and the -CF_2-CFX- units. Crosslinking can be obtained via reaction with OH functionality in FEVE with polyisocyanates.

FEVE fluoropolymer resins can be distinguished based on their use in solvent-borne (SB) or water-borne (WB) formulations, which also influences the barrier properties of the coatings. Swartz et al. [7], for example, showed by electrical impedance spectroscopy (EIS) of methyl methacrylate coatings that water uptake is greater for WB coatings compared to SB coatings. Increased water uptake is a significant drawback because WB formulations are currently favoured for environmental reasons.

One issue regarding protective coatings for bronze works of art is their removability (Fig. 1A), which is a critical ethical guideline for materials used in conservation. The application of organic strippers based on benzyl alcohol cannot remove compact SB or WB fluoropolymer coatings. If removability of coatings is required, the structure of the coatings must be

modified. Approaches to allow adequate removability include the addition of releasing co-solvents [12], incompletely crosslinked polymeric structures (NCO:OH ratio below 1), pendant carboxylic groups [13], the use of polyisocyanates with hydrophilic character [8] and the addition of agents that impart greater strippability to coatings [14]. Such agents include compounds that have a phenyl group close to hydroxyl or aldehyde groups or agents containing oxygen (alcohols, esters, or aldehydes).

(ii) Analytical aspect. Infrared (IR) and Raman spectroscopy are applied in the field of cultural heritage and modern art materials due to their potential for non-invasive measurements [2,15,16,17,18,19]. Examples include the identification of pigments and degradation mechanisms in works of art, such as atmospheric corrosion [20,21,22] and the determination of trade routes [15]. However, for the development of protective coatings for metal/alloy art objects, more informative yet more invasive studies of coatings exposed to weathering are needed. One interesting example is an IR spectroscopic comparative study of Incralac™ and SB and WB acrylic urethane coatings deposited on copper and bronze substrates [23]. An even more accelerated approach is represented by IR/Raman spectroscopy combined with an electrochemical technique either *ex situ* or *in situ*, which can be used to follow the processes of the degradation of protective coatings during forced anodic polarisation (Fig. 1B). This approach is destructive but provides information about the behaviour of protective coatings during long-term outdoor exposure and the bonds in the coatings that are the most prone to cleavage. Modifications to the coating components and the structure can be made iteratively, leading to more efficient protective coatings.

IR RA spectroscopy is a technique used for the *ex situ* IR measurements (Fig. 1B) of coatings, in which a P-polarised IR beam falls to the coating/reflective substrate in tandem under the near-grazing incidence angle (NGIA) of 80° [24]. Longitudinal (LO) modes that appear in IR RA spectra are mostly shifted towards higher wavenumbers and can also reflect changes in the shape of the bands. These shifts are much larger in the case of inorganic modes compared to organic modes [24]. Calculation of these shifts is possible for ordered crystalline structures, whereas there is a debate concerning disordered materials [25]. An *ex situ* IR RA technique has already been used to follow degradation of sol-gel protective coatings on aluminium alloys [26,27,28,29,30], providing information about the hydration of coatings, breakage of siloxane modes and consequent re-formation of silanol groups. A challenging question remains regarding what changes would be observed on other types of polymeric protective coatings.

A disadvantage of the described *ex situ* IR RA measurements (Fig. 1B) is the contact of coatings with the atmosphere, i.e., the coating is first chronocoulometrically charged in the electrochemical cell and then transferred to the sample compartment of the IR spectrometer. This obstacle can be overcome by the application of *in situ* Raman measurements (Fig. 1B), during which the protective coating on the substrate is constantly immersed in the electrolyte. Such measurements are made in a three-electrode *in situ* cell in which the working electrode is bronze-coated with a given coating that must be thick enough (in the μm range) to enable the detection of Raman scattering [28,30]. This might be the reason that *in situ* Raman studies on sol-gel protective coatings for aluminium alloys mostly revealed the changes in the intensity of bands and the formation of pits at high anodic potentials [28,30].

Accordingly, herein we describe the preparation and characterisation of four different protective coatings for patina-free bronze on the basis of FEVE fluoropolymers: two from SB formulations and two from WB formulations (Fig. 1A). The first type of SB coating was intentionally prepared with a hydrophobic, compact and irremovable structure (designated WB-c). The other type of SB coating possessed a looser structure (designated SB-h), due to the application of agents that impart strippability, to achieve removability. Similarly, the first type of WB coating was made with a compact structure (designated WB-c). The second type of WB coating was modified with the addition of hydrophilic polyisocyanate with the aim of loosening its structure to achieve removability (designated WB-h). Characterisations of the surface morphology and roughness of the coatings were performed using scanning electron microscopy (SEM), energy dispersive X-ray spectroscopy (EDS), and atomic force microscopy (AFM), and the contact angles were determined by tensiometry. The protection efficiency of the coatings was investigated using a potentiodynamic polarisation technique and combined electrochemical and vibrational spectroscopic techniques (*ex situ* IR RA and *in situ* Raman spectroelectrochemistry). Both techniques were combined to follow the evolution of the coatings' structure during forced anodic polarisation to better understand the coatings' degradation paths.

2. Experimental procedure

2.1. Preparation of coatings

Fluoroethylene/vinyl ether (FEVE) alternating copolymers produced by AGC (Asahi Glass Company) Japan (Lumiflon products) were used to produce four types of coatings, i.e., two types of SB formulations and two types of WB formulations (Fig. 1A, Tables 1,2).

SB coatings. The first type of SB formulation was prepared to deposit a hydrophobic, compact and irremovable coating (designated as SB-c). The formulation for the second type of SB coating (designated as SB-h) was intentionally modified by the introduction of agents that can impart strippability. Both SB coatings were prepared from the fluoropolymer resin Lumiflon 200 and crosslinked with the poly(isocyanate) hardener Desmodur n75 at a molar ratio of 1.5:1 (SB-c) and 1:1 (SB-h) in butyl acetate solvent (Table 1). Trisilanol-heptaisooctyl-polyhedral oligomeric silsesquioxane (POSS) was introduced to both SB formulations to increase scratching, thermic and chemical resistance. Trisilanol-heptaisooctyl-POSS is an open silica cage with an inorganic silsesquioxane core and organic isooctyl groups attached at the corners of the cage. The open cage structure offers three silanol functionalities for binding into the coating matrix. Tinuvin 1130 and Tinuvin 292 were applied as light stabilisers. Tinuvin 1130 is a hydroxyphenyl benzotriazole-based liquid UV absorber that can be used in combination with a light stabiliser of the sterically hindered amine class, in our case, Tinuvin 292. Consequently, synergistic effects can impart superior coating protection regarding blistering, gloss reduction, cracking, colour change and delamination. In the formulation for compact SB-c coating, only an additive for levelling Byk 3441 was added; 2-(2-methoxyethoxy)acetic acid, methyl lactate and tetraethylene glycol were applied to soften the SB-h coatings. All chemicals were used as received.

WB coatings. Both WB coatings were produced from Lumiflon 4400 resin, which was dispersed in water. The first type of WB coating was prepared as a compact coating that would be irremovable (designated as WB-c coating). The second type of WB coating was modified with the aim of achieving removability with the addition of hydrophilic polyisocyanate (designated as WB-h). In both WB formulations, additives for levelling and defoaming were introduced, and Tinuvin 5333-DW was used as a UV absorber. Tinuvin 5333-DW is an aqueous dispersion of a blend of UV absorbers and a hindered amine light stabiliser. Compact coating WB-c was crosslinked with polyisocyanate Easaqua XD 401, which was added at a molar ratio resin:polyisocyanate of 1:1. In the WB-h coating, an equal

part of aliphatic anionic polyurethane resin Bayhydrol UH 340/1 was applied in addition to Lumiflon 4400. The surfactant polyol agent Pluronic 127 was used to facilitate solubilisation in water, and the whole formulation was crosslinked with hydrophilic aliphatic hexamethylene diisocyanate (HDI)-based polyisocyanate Bayhydur XP 2655. All chemicals were used as received.

Both SB and WB coatings were produced as two-component formulations, which means that the polyisocyanate was added to the other components 30 min before the production of the coatings and stirred using a dispermat dissolver. The formulations were then deposited on bronze discs using a spin coating technique (1st step: 5 s, 500 RPM; 2nd step: 60 s, 700 RPM). After deposition, the coatings were thermally treated at 60 °C for 1 h and then left for at least 3-4 days at room temperature before any measurements.

Bronze rods 85 555 with a diameter of 3 cm were obtained from Casa Del Bronzo Srl (Brescia, Italy) and cut into discs with a thickness of 3 mm. Prior to deposition, the surface of the discs was ground with P1200 grit SiC abrasive paper, followed by polishing with two diamond pastes with particle sizes of 9 and 3 μm.

Removability of coatings was tested using a stripper composed of benzyl alcohol, tetraethylene glycol and Triton X100. The SB-h and WB-h coatings could be removed with this stripper.

2.2. Rheological characterisation of formulations

The rheological measurements were performed using a Physica MCR301 (Anton Paar) rotational controlled rate rheometer equipped with a cone and plate sensor system (CP 50/2°). Standard rotational flow tests were performed with a triangular method by changing the shear rate from 0 - 1000 - 0 s^{-1}. To simulate the three steps to which the paint is subjected (storage in the container, deposition on the substrate and the formation of dry film), three-step time tests were performed under oscillatory shear conditions. In the 1st and the 3rd steps, the paint was subjected to conditions with no shear; these two steps were performed at a constant deformation, small enough not to destroy the structure of the sample. In contrast, the 2nd step simulated the process of application; therefore, the paint was subjected to high shear, and a

high degree of deformation was applied in this step. All rheological measurements were performed at a constant temperature of 23 °C, which was also the temperature used for spin-coating.

2.3. Characterisation of bronze discs and coatings

An X-ray diffractometer (XRD) PANalytical X'Pert PRO ($CuK_{\alpha 1}$ = 1.5406 Å) with completely open X'Celerator detector (2.122° 2Θ) was used for recording the XRD pattern of bronze. The XRD pattern was measured from 5 to 100° 2Θ with a step size of 100 s.

The thickness of SB and WB coatings was determined using a Taylor Hobson Series II profilometer. The steps that were used for measurements were created by the removal of sticky tape that was used to affix the substrate to the spin-coater rotating table. The profilometer tip was then dragged three times over the steps, and the average thickness value was calculated.

Static contact angles for water, diiodomethane and formamide were recorded on a theta tensiometer (Biolin Scientific) at room temperature. A 4 μL drop of each liquid was deposited on the coating using a microsyringe, and determination of contact angle was repeated three times at different positions on the coating. One Attention software was used to determine contact angles from images obtained with a digital video camera. Surface energy values were calculated according to the method of van Oss [31] from the average values of contact angles obtained for each of the liquids with known total surface energy value σ^{tot}, dispersive part σ^{LW}, electron donor component σ^{+} and the electron acceptor component σ^{-} by solving a set of three complete Young equations.

To record the transmittance spectra of the coatings, they were deposited on one side of glass slides. Transmittance spectra were measured using a UV-VIS-NIR Perkin Elmer Lambda 950 spectrophotometer in a spectral range from 250 to 2500 nm. The spectra were measured for initial coatings and coatings exposed in a Suntest chamber (160 W/m^2) for 135 and 670 h. The optical quality of the coatings was estimated via the haze value, which is defined as the ratio

of diffuse to total transmittance in the 380 to 780 nm range according to ASTM test method D1003.

2.4. Electrochemical and accelerated corrosion tests

Potentiodynamic polarisation curves were recorded with an Autolab PGSTAT 302N potentiostat-galvanostat in a flat cell K0235 (Princeton Applied Research) filled with 0.5 M NaCl electrolyte. The bronze disks with protective SB or WB coating were mounted as working electrodes with a geometrical area of 1 cm^2. The Pt grid counter electrode was positioned opposite to the coating and the $Ag/AgCl/KCl_{sat}$ reference electrode was positioned in the near vicinity of the working electrode. During measurement, the coating was first held for 30 min at an open circuit potential, followed by linear sweep voltammetry with a scan rate of 1 mV s^{-1} from -1.5 to 1.0 V.

Accelerated corrosion tests were carried out by exposing the coated bronze disks in a closed glass vessel to an aqueous 1M HCl solution at 50 °C. The disks came in contact only with the acid vapour; they were not in direct contact with the aqueous solution. The procedure is described in detail in Ref. [5,32]. The coatings were characterised before and after 3 h of exposure to the aggressive species. Morphological characterisation was performed by means of an SEM Cambridge 360 microscope equipped with a LaB6 filament equipped with an energy dispersive X-ray spectrometer (EDS) INCA 250. Optical images were recorded by using a Leica MEF4M microscope equipped with a digital camera (Leica DFC 280).

2.5. *Ex situ* IR RA and *in situ* Raman spectroelectrochemistry

The Autolab PGSTAT 302N potentiostat-galvanostat was also used for *ex situ* IR RA spectroelectrochemical measurements. The edges and the back of bronze disks with deposited coating were protected with an epoxy shield. This shield was prepared from Epofix resin, which was cured using Epofix hardener (Struers company) and left for 24 h at room temperature to dry. The coating was then treated in an electrochemical cell with a chronocoulometric technique. The electrolyte used was 0.5 M NaCl. The coating was charged at certain values of potential from -0.8 to 0 V for 240 s (and up to 1920 s). After each

chronocoulometric charge, the sample was taken from the electrochemical cell, washed with distilled water, dried and moved to the Bruker spectrometer IFS 66/S for IR RA measurement in a reflectance accessory (Specac) with P-polarised light at a near-grazing incidence angle of 80°. The resolution of measurements was 4 cm^{-1}. All IR RA spectra were measured relative to a gold plate background.

In situ Raman spectroelectrochemical measurements were performed on a WITec alpha 300 confocal Raman spectrometer and Autolab PGSTAT 302N potentiostat-galvanostat. The round custom-made three-electrode *in situ* Raman cell was designed from Teflon and is described in Ref. [28]. The bronze with a coating with dimension 1×5 cm^2 was mounted as a working electrode, and its edges were protected with paraffin. $Ag/AgCl/KCl_{sat}$ served as the reference, and a Pt grid served as the counter electrode. The cell was filled with 0.5 M NaCl electrolyte. The laser excitation wavelength was 532 nm, and the objective magnification was 20×. Single Raman spectra were recorded at a single spot on the coating with 50 scans after chronocoulometric charging at potentials of -1.2 V (240 s) and 0 V (2400 s). The image was recorded in dimensions of 5×5 μm^2 using 50 points per line and 50 lines per image, with a scan speed of 25 s $line^{-1}$, an integration time of 0.5 and 1 scan at each point.

3. Results

3.1. Composition of bronze discs

EDS measurements showed an uneven distribution of elements in the bronze disc. When the EDS spectrum was recorded over a large rectangular part of the disc surface (spectrum 1 in Fig. S1 in Supporting information), the concentration variance of alloying elements was as high as 6 wt.% (Table 3). In contrast, spectra 2 and 3, which were recorded on spots, showed an increased concentration of lead. Because lead has essentially no solid solubility in copper-based alloys, Pb appears in the form of fine particles in bronze [33]. The size of these particles and their distribution are dependent on the cooling process during bronze production. The information depth of EDS is approximately 2-3 μm, so these results mostly reflect the surface characteristics of the bronze. This is probably the reason that carbon was also detected in some EDS spectra: the time-consuming determination of EDS spectra can lead to carbon contamination of the surface, and such contamination can also occur during surface

preparation. Although the surface composition is significant for coating deposition and studies of their degradation, the bulk concentrations of elements give representative values for bronze 85 555, being much closer to approximately 5% Sn, Zn and Pb (Table 3).

The XRD pattern of bronze confirmed the findings from EDS (Table 3). The presence of Cu (Fig. 2A) was detected based on the XRD pattern of a pure Cu plate (PDF 00-004-0836). In bronze 85 555, Pb is the only additive that appears in elemental form (PDF 03-065-2873), which also corresponded to the areas of high Pb concentration as determined by EDS (Table 3). Sn and Zn formed phases with Cu, which was inferred from the positions of shoulders that appeared as low-2Θ and high-2Θ tails of Cu peaks. These positions were close to $Cu_{13.7}Sn$ (PDF 03-065-6821) and Cu_3Zn (PDF 03-065-6567), but precise identification was not possible due to large overlaps in the diffractions and large sampling areas.

Prior to the thermal treatment of the protective coating on bronze, the bronze itself was examined regarding its behaviour under increasing temperatures. The bronze disk was gradually heated to 60, 80, 100, 150, and 200 °C. Fig. 2B reveals that the IR RA spectrum recorded after thermal treatment at 150 °C shows a low-intensity band at 648 cm^{-1}, which increased in intensity after heating at 200 °C. Such band in IR RA spectra can be ascribed to the formation of Cu_2O [23,34]. These measurements confirmed that the thermal treatment of deposited coatings at 60 °C does not influence the bronze itself and is consequently safe for coating preparation.

3.2. Rheological properties of SB and WB formulations

With the aim of depositing coatings with good quality, rheology parameters were studied for all resins and the selected SB and WB formulations. The dependence of viscosity on the shear rate was determined with flow tests in two steps: increasing shear rate from 0.01 to 1000 s^{-1}, followed by decreasing the shear rate from 1000 s^{-1} back to 0.01 s^{-1} (Fig. 3). In the shear rate range studied, the resin used for SB coatings (Fig. 3A) exhibited detectable shear thinning behaviour at high values of shear rate. In contrast, due to the addition of solvent and other components, both prepared SB coatings exhibited Newtonian flow behaviour with a significantly lower viscosity (0.01 Pa.s). This viscosity enabled the preparation of thin films on the selected substrate. A similar viscosity was also observed for the WB coatings (Fig.

3B). The resins used for the preparation of WB coatings exhibited higher viscosity with detectable shear thinning behaviour, whereas the viscosity of the prepared formulation was Newtonian and in the similar range as the SB coatings, i.e., a range that enabled spin-coating deposition on the bronze substrate. The dependence of the viscosity on the shear rate was time-independent for all examined formulations.

In addition to the standard rotational flow tests, three-step time tests were performed to simulate the three steps to which the formulation is subjected: storage in the container, deposition on the substrate, and the formation of the dry coating. In the 1st and 3rd steps, the formulation is subjected to the conditions with no shear; therefore, these two steps were performed at a constant small deformation, whereas in the 2nd step — during the application — the formulation is subjected to high shear; therefore, high deformation was applied. The results of these tests for the resins and the selected SB and WB formulations are presented in Fig. 4. The resin for the preparation of SB coatings exhibited viscoelastic liquid-like behaviour with a characteristic drop of consistency (viscosity and dynamic moduli (G', G'')) in the 2nd step of the test, which corresponded to the conditions during the application. The resin LF 4400 exhibited only a viscous contribution (G'') to viscoelastic behaviour with G' = 0. However, the drop in G'' was still observed in the 2nd step of the experiment, indicating lower viscosity at a higher shear rate range, as was also observed with flow tests (Fig. 3). In the 3rd step, the dynamic moduli of the WB resins Lumiflon 4400 and Bayhydrol UH 340/1 returned to their initial values, although a delay in recovery was observed for the SB resin Lumiflon 200. In contrast, the prepared coating formulations exhibited Newtonian behaviour with the same values of dynamic moduli during all three steps of the experiment. Such rheological behaviour is not preferred for coatings that should be applied with a spraying technique. However, the priority of our research was to develop coatings that would be removable and applied with a spin-coating technique. In the future, the rheological characteristics of the formulations will be tailored in the way that the coatings could be applied via brushing.

3.3. Surface and optical characteristics of protective coatings

Fig. 5 depicts SEM and AFM micrographs of coatings deposited from the SB and WB formulations. SEM micrographs of both types of SB protective coatings revealed a

homogeneous surface with low roughness. AFM images confirmed this finding, revealing a surface roughness of 85 and 70 nm for SB-c and SB-h coatings, respectively. In contrast, SEM of WB coatings revealed a more inhomogeneous surface, with clearly recognisable defects. The levelling was also not as complete as for the SB coatings. Surface roughness calculated based on AFM images reached significantly higher values of 270 nm for WB-c and 295 nm for WB-h.

The application of protective coatings for art objects requires that they be highly transparent, homogeneous, and without defects. Their toxicity should be as low as possible, and importantly, they should also remain transparent after accelerated ageing, i.e., exposure in a Suntest chamber. Consequently, UV absorbers and light stabilisers of the sterically hindered amine class are added with the aim of preventing or significantly diminishing photooxidation reactions. Fig. 6 shows the transmittance spectra of SB and WB coatings in the initial state and after exposure to UV ageing for 135 and 670 h. The initial WB coatings had higher transmittance mostly at short wavelengths (below 1000 nm) compared to SB coatings. After exposure in the Suntest chamber, the transmittance of WB coatings remained practically unchanged, whereas a drop of 1–2% below 1000 nm was noted for SB coatings.

The hydrophobicity of coatings is highly connected with the protection effectiveness. The contact angle for water is 104.6° for uncoated bronze. The surfaces became even more hydrophobic after the application of SB coatings, i.e., 105.9° for SB-c and 106.0° for SB-h coatings (Fig. 7). This indicated good crosslinking of the fluoropolymer resin (Lumiflon 200) with the polyisocyanate hardener. However, these values are still somewhat lower compared to ~112° obtained when the fluorine-bearing compound was introduced into the polydimethylsiloxane matrix [35]. It was unexpected that the WB coatings would have much lower contact angles for water: the contact angle was 78.6° for WB-c coatings and only 57.5° in the case of the WB-h coating. Both WB coatings showed more hydrophilic properties despite also being prepared from the fluoropolymer (Lumiflon 4400). This showed how different the characteristics of fluoropolymer resins in the SB or WB formulations were. Surface energy values (Fig. 7) were similar and in the range of 34.1 – 31.2 mJ cm^{-2} for bronze as well as both SB and WB-c coatings. The highly hydrophilic character of the WB-h coating and its susceptibility to water is reflected in the highest free surface energy value of 56.0 mJ cm^{-2}. This high value is also a consequence of the introduction of a surface-active agent and hydrophilic polyisocyanate.

3.4. Potentiodynamic polarisation and accelerated corrosion test of coatings

The contact angles for water and surface energy values considerably influenced the electrochemical behaviour of SB and WB coatings. In Fig. 8, the potentiodynamic polarisation measurements of bare bronze and bronze covered with both kinds of SB and WB coatings are depicted. The measurements showed that the cathodic current density of SB coatings decreased by 1–2 orders of magnitude, whereas these decreases reached 4–5 orders of magnitude for anodic current densities. Across the whole range of potential, the current density was lower for the SB-c coating, which was expected due to its more compact structure compared to the SB-h coating. In the case of WB coatings, a decrease in current density was noted only at potentials above the corrosion potential. Specifically, anodic current density decreased by about two orders of magnitude for the compact WB-c coating, but the decrease was below one order of magnitude for the hydrophilic WB-h coating. We concluded that potentiodynamic polarisation measurements (Fig. 8) confirmed the difference between SB and WB coatings. SB coatings offered higher protection effectivity compared to WB coatings. In addition, the compact coatings (SB-c and WB-c) were somewhat more protective compared to coatings intentionally designed to have more hydrophilic character (SB-h, WB-h), which would be more easily removable from works of art.

In addition to potentiodynamic polarisation, an independent treatment in the form of an accelerated corrosion test was used to assess the protective efficiency of the developed coatings. This method was intentionally developed for the evaluation of water-soluble protective coatings, which is also interesting from the conservation point of view [5,32]. In this experiment, all coatings were exposed to acidic vapours at 50 °C for 3 h. To evaluate their ability to inhibit the degradation of the alloy substrates, the coatings were observed using optical microscopy (Fig. 9) and SEM (Fig. 10) before and after the test. As electrochemical measurements, the results of the accelerated corrosion test also clearly showed the superior performance of SB coatings over WB coatings. Specifically, the SB coatings resulted in stable, transparent, and effective coatings after the 3 h exposure to acidic vapour. In contrast, in the case of WB coatings, the accelerated corrosion treatment led to the loss of the coatings' transparency and to modification of the coatings' appearance (Figs. 9 C2, D2).

It is worth noting that the best performance was obtained with the hydrophobic compact SB-c coating (Fig. 9 A1, A2). The optical micrographs remained practically unchanged after exposure, and there is no evidence for the formation of corrosion products, demonstrating the efficiency of the SB-c coating in the inhibition of corrosion processes. Moreover, SEM images obtained after the accelerated corrosion test (Fig. 10) demonstrate the difference between the SB-c and SB-h coatings. Aggregates larger than ten microns were observed within the treated SB-h coating (Fig. 10 B2), whereas significantly smaller aggregates were detected in the SB-c coating (Fig. 10 A2). Further investigations using EDS analysis (Fig. 10C) revealed the presence of C, O, F, Cl and Si from POSS, and Pb and Cu from bronze 85 555, when measured on the aggregate, which is circled in Fig. B2. As shown previously, Pb exists in the form of fine particles in bronze that were evident from EDS (Table 3, Fig. S1) and XRD measurements (Fig. 2A). During the test, the coating was exposed to a chloride-containing atmosphere (0.1 M HCl_{aq}). Consequently, the corrosion products likely formed through localised attack of chloride ions [19,33]. It has been confirmed for archaeological bronzes that corrosion takes place towards the bulk along the lead islands [33].

In conclusion, the findings from electrochemical measurements and the accelerated corrosion test demonstrated that SB coatings are more effective than WB coatings in the protection of copper-based alloy substrates. Moreover, compact coatings are more protective than hydrophilic coatings. Specifically, the SB-c coating with the most hydrophobic and compact structure exhibited the best protective performance, maintaining a stable structure and able to hinder any surface modification during the accelerated corrosion test. Deeper structural investigations that could provide further insights into the corrosion processes during forced anodic polarisation were performed using *ex situ* IR RA and *in situ* confocal Raman spectroelectrochemistry.

3.5. *Ex situ* IR RA spectroelectrochemical studies

The aim of *ex situ* IR RA spectra measurements (Fig. 11) is to obtain information about the stability of protective coatings during forced anodic polarisation, which was used to simulate long-term outdoor exposure. This technique is relative, mainly giving an estimation of the protective effectivity of coatings compared to others tested in the same way. Information that can be obtained through changes in the bond positions or intensities in the *ex situ* spectra

reflects which bonds are most prone to change or even cleavage. In this way, iteratively, the components of coatings can be modified, leading to improved performance. This approach has been shown in the case of sol-gel protective coatings [26,27,28,29,30]. In the case of organic polymeric coatings, prepared based on commercial products with compositions that are not completely known, the identification of spectral bands is not so straightforward.

Ex situ IR RA spectra were recorded for all four prepared coatings after chronocoulometric charging at specific potentials from -1 to 0.8 V (Fig. 11). The interferences that appeared in the SB coating spectra (Fig. 11A, B) showed that the coatings were too thick for measurements under near grazing incidence angle conditions. This approach was valid mainly for SB-c coating, in the spectra of which the bands were also slightly blurred (Fig. 11A). The spectra of coatings did not show the presence of the isocyanate mode at 2240 cm^{-1}, indicating that no unreacted groups of polyisocyanate hardener remained present in the coatings.

Comparison of the *ex situ* spectra of SB-c, SB-h and WB-c coatings revealed that the bands in the spectra remained in their positions during polarisation (Fig. 11A, B, C). Eventually, at more positive potentials, slight decreases in the intensity of the bands occurred. These decreases have been observed in *ex situ* IR RA testing of sol-gel coatings [26,27,28,29,30] and occur due to manipulation of the coatings outside the electrochemical cell (repeated cleaning and drying). The assignments of some characteristic bands in the spectra are given in Table 4. The IR RA bands at 2929–2962 and 2875–2860 cm^{-1} were assigned to asymmetric and symmetric CH_2 stretching, and CH_2 bending appeared between 1470 and 1440 cm^{-1}. The bands in the range of 1111–1163 cm^{-1} comprise the CF_2 and C-O groups of the resins. The 1800–1600 cm^{-1} region represents the -NH-CO-O- bonds that form from reactions between OH groups of the resin and the NCO groups of polyisocyanate. In this region, the band of free C=O groups appeared as a shoulder at 1765–1741 cm^{-1} [36]. The most intense band evolved at 1691–1682 cm^{-1}, indicating hydrogen-bonded C=O groups. Different types of hydrogen-bonded C=O groups resulted in two additional shoulder bands (Table 4).

In contrast, the hydrophilic WB-h coating behaved differently (Fig. 11D). Hydration of this coating was extensive at the cathodic potential, which is consistent with the more hydrophilic nature of this coating (Fig. 7). High amounts of water uptake is associated with WB coatings based on methyl methacrylate, and the water uptake increases with coating thickness [7]. In contrast, similar SB coatings absorbed approximately 5% of their dry mass independent of

thickness [7]. In the 1800–1600 cm^{-1} spectral region (Fig. 11D), the intensity of the 1741 cm^{-1} band of free C=O groups approached the most intense hydrogen-bonded C=O mode at 1685 cm^{-1}. This indicated that more free C=O groups were present compared to the other coatings (SB-c, SB-h, WB-c in Figs. 11A-C). *Ex situ* IR RA of the coatings further showed a decrease in the intensity of all bands with increasing anodic polarisation, reflecting the slight gradual dissolution of the hydrophilic WB-h coating. After polarisation at 0.8 V for 240 s, pitting of this coating became obvious, and the *ex situ* IR RA spectrum revealed a broad band at approximately 656 cm^{-1} [34]. Such a band indicated the formation of Cu_2O on the surface of the bronze. Formation of oxide below the sol-gel protective coating has been observed by *ex situ* IR RA spectroelectrochemistry of the aluminium alloy AA 2024 [26].

3.6. *In situ* Raman spectroelectrochemical studies

In situ Raman measurements were performed on WB-h and SB-h coatings (Figs. 12,13). Due to their less compact structure, we expected that degradation would occur more quickly in comparison to compact WB-c and SB-c coatings. The thicker WB-h and SB-h coatings were produced using deposition with a hand coater (wet coating thickness set to 24 μm) with the aim of alleviating the detection of Raman bands. Fig. 12A depicts the scheme of the three-electrode *in situ* Raman cell [28], in which the bronze-coated with a given coating was set as a working electrode.

Optical imaging of the initial hydrophilic WB-h coating in 0.5 M NaCl electrolyte (Fig. 12B) revealed a homogeneous coating surface, and in the small red square in its middle, the Raman image (Fig. 12C) was measured. This image was averaged to the stretching ν(C-H) modes, and the exchange of bright or dark shades indicates higher or lower content, respectively, of the groups concerned, i.e., the intensity of their bands, at those positions. The bright/dark pattern in the initial Raman image corresponds the slight indentations that remained after polishing with diamond pastes. The intensities were the largest in the bright spots of the Raman image, as depicted by the spectrum in Fig. 12D. The higher noise in this spectrum arose from the fact that Raman images are usually measured using one scan for the detection of the Raman spectrum at each position of the image. The number of scans used was considerably lower compared to the 50 scans usually used for recording a single Raman spectrum in one spot. Raman imaging exposes the surface of coatings to the laser for

considerably more time than a single Raman spectrum measurement, consequently; it can lead to burning of the coatings.

After detection of the initial state of the coating, it was exposed to two different potentials. First, to a potential of -1.2 V (240 s) before the corrosion potential of the coating, and second, to the potential of 0 V (240 s), after the corrosion potential. The initial state and both potentials used for chronocoulometric charging of the coating are marked with arrows in Fig. 12E. The corresponding single Raman spectra are depicted in Fig. 12F and were scaled to the stretching ν(C-H) modes. In the single Raman spectrum of the initial WB-h coating (Fig. 12F), the broad band at ~3300 cm^{-1} was due to the electrolyte. The C-H stretching modes of CH_2 appeared between 2950 and 2850 cm^{-1} [37] (Table 5). Bending of CH_2 groups overlapped with the NCO mode, the latter being reported in the literature at 1448 cm^{-1} [37,38]. The presence of an NCO band indicated that not all polyisocyanate groups crosslinked with the OH groups of the resin, which was a consequence of the high coating thickness. However, the appearance of the band at 1760 cm^{-1} confirmed that crosslinking formed through a -NH-CO-O- bond [37]. The coupled ν(C-N) and ν(C-O) stretching vibrations appeared at 1235 cm^{-1} [37].

The electrochemically treated spectra did not show any changes in intensities or shifts in band positions. Regardless, when an additional chronocoulometric pulse at 0 V for 720 s was applied, the hydrophilic WB-h coating softened, the adhesion worsened, and the surface became uneven in optical images. This made further Raman measurements impossible because any application of the laser induced burning.

Raman images of initial SB-h coating in electrolyte revealed the homogeneous distribution of vibrational groups. After application of 0 V (2400 s), black spots started to appear on the surface of the SB-h coating. Consequently, measurement of single Raman spectra was performed on the coating (Fig. 13A) and at the black spot in Fig. 13B. Comparison of the Raman spectra showed the same bands, and the intensity of the bands was similar. In the SB-h coating, we also noted some unreacted NCO groups (1448 cm^{-1} [37,38]) due to the larger coating thickness prepared for *in situ* Raman measurements. However, the spectra that were recorded at the sites of black spots comprised, in addition to the bands of the coating, one more band at 1057 cm^{-1}.

The origin of this band is not clear. The band positions of oxidised species of the copper surface were found at much lower Raman shifts, as shown by *in situ* Raman [39,40] and *in situ* surface-enhanced Raman [41,42] spectroscopy studies of copper in various electrolytes. The bands for Cu_2O were detected at 633, 492, 411 and 297 cm^{-1}, $Cu(OH)_2$ at 488 and 292 cm^{-1} and CuO at 635, 347 and 250 cm^{-1} [39], similar in Ref. [40] (both studies used a 488 nm laser excitation line). Additionally, the band assigned to the adsorption of chloride from KCl media to the copper surface was at 290 cm^{-1} [42].

However, according to the results of EDS obtained from the SB-h coating after the accelerated corrosion test, Pb and Cl are present in aggregates (Fig. 10C). Studies of Raman signatures of Japanese/Chinese bronze patina [2] suggest the formation of phases with Pb, for example, $PbSO_4$, also having a band at 1060 cm^{-1}. Eventually, $PbCl_2$ could form on SB-h coatings, but the observed Raman shifts of monocrystalline $PbCl_2$ [43] are below 180 cm^{-1} and not observed in our spectra (Fig. 13C). Frost et al. [44] reported the Raman spectra of various lead minerals, i.e., $Pb_3(CO_3)_2(OH)_2$, $Pb_2CO_3Cl_2$, Pb(OH)Cl and $PbCO_3$. According to these Raman shifts and due to exposure of our coating to aqueous electrolyte and the presence of C and O in the EDS spectrum (Fig. 10C), lead carbonate (1484, 1369, 1053, 685 cm^{-1} [44,45]) is tentatively suggested to form on black spots of SB-h coating. However, formation of other mixed phases in addition to $PbCO_3$ cannot be excluded.

4. Discussion

Due to environmental and toxicological aspects, exchanging SB protective coatings with WB coatings seems extremely attractive. From practical points of view, as well as regarding the protection efficiency, such an exchange is more questionable, especially in the case of the outdoor protection of bronze monuments: this protection should be highly durable, and coatings should resist weather conditions. Direct comparison of SB and WB coatings for protection of bronze has been performed on co-polymer resins of methyl methacrylate [7]. That work confirmed the greater water uptake of WB coatings compared to SB coatings.

The greater water uptake of WB coatings was also confirmed herein for fluoropolymer coatings by *ex situ* IR RA measurements (Fig. 11). The broad OH band that developed after contact with an electrolyte was followed at high anodic potentials by the formation of a 656

cm^{-1} band (Cu_2O) due to the oxidation of the bronze (Fig. 11D). The reason for this could be the lower degree of crosslinking in the hydrophilic WB-h coatings (Fig. 11D) compared to other coatings (Fig. 11A-C). Specifically, in the 1800–1600 cm^{-1} spectral region characteristic of -NH-CO-O- crosslinking, bands corresponding to free and hydrogen-bonded C=O groups appeared (Table 4). In the IR RA spectra of the WB-h coating, approximately equally intense bands of free C=O groups at 1741 cm^{-1} and hydrogen bonded C=O at 1685 cm^{-1} were noted. In contrast, in the IR RA spectra of all other coatings (Fig. 11A-C), the hydrogen-bonded C=O band at ~1685 cm^{-1} was the most intense, whereas the band corresponding to free C=O groups was present as a very low-intensity shoulder.

All experiments confirmed the better protection efficiency of SB coatings compared to WB coatings. This was also true when considering SB and WB coatings with somewhat different thicknesses, which behave as barrier coatings. SEM images (Fig. 5E, G) showed that WB coatings were not completely homogeneous, which was reflected in their high degree of deterioration when exposed to the accelerated corrosion test (Fig. 9C, D) and potentiodynamic polarisation (Fig. 8B). More water uptake by WB coatings is connected with lower contact angles for water, i.e., 78.6° for compact WB-c and only 57.5° for hydrophilic WB-h coatings (Fig. 7). Values of contact angles for SB coatings were above 105.9° (Fig. 7).

Moreover, *in situ* Raman measurements also showed that long-lasting chronocoulometric charging above the corrosion potential is more damaging to the WB-h coating (Fig. 12) compared to the SB-h coating (Fig. 13). Specifically, charging the WB-h coating at 0 V for 720 s resulted in the softening of this coating and its detachment from the bronze disk substrate, whereas SB-h remained adhered to the bronze even after 2400 s of treatment at the same potential. To some extent, the lower performance of WB coatings can be ascribed to the lower thickness, but the large differences also indicated structural characteristics. An important finding of *in situ* Raman spectroelectrochemistry is the eventual formation of lead carbonate at high anodic polarisations of the SB-h coating (Fig. 13C). Large concentrations of Pb and Cl were found together with other elements (C, O, Si, F, Cu) in aggregates that formed at the surface of SB-h coatings during an accelerated corrosion test (Fig. 10). This suggests that chloride ions locally attached to the bronze along Pb islands (Table 3, Figs. 2A and S1), leading to the formation of corrosion products. In contrast, the bronze/coating tandem is exposed to the aqueous electrolyte during the *in situ* Raman spectroelectrochemical measurement. Aqueous electrolytes are often reported to stimulate the formation of

carbonates. The presence of a 1057 cm^{-1} band together with vibrations between 1480 and 1310 cm^{-1} could support this idea, i.e., the formation of lead carbonate at certain spots on the coating.

5. Conclusions

Four types of protective coatings based on FEVE fluoropolymers for bronze were prepared, i.e., two types of SB coatings and two types of WB coatings. The first SB coating was made as a hydrophobic compact coating (SB-c). The second SB coating (SB-h) was modified with the addition of agents that imparted strippability. Similarly, the first WB coating was made as a compact coating (WB-c), and the second WB coating was modified by the addition of hydrophilic polyisocyanate (WB-h) in accordance with removability considerations for the protection of art objects. The properties of the coatings were evaluated using various analytical techniques, including combined electrochemical and vibrational spectroelectrochemistry.

Rheology characterisations of SB and WB formulations revealed that all formulations exhibited Newtonian flow behaviour with viscosities of 0.005 – 0.01 Pa.s. This enabled the deposition of homogeneous SB coatings with low surface roughness (85 and 70 nm). WB coatings, on the other hand, were more inhomogeneous and had higher roughness (270 and 295 nm). SB coatings possessed significantly higher static contact angles for water (105.9° (SB-c), 106.0° (SB-h)) compared to more hydrophilic WB coatings (78.6° (WB-c), 57.5° (WB-h)). Consequently, SB coatings offered better protection than WB coatings. The accelerated corrosion test, i.e., exposure of coatings to acid vapours, confirmed the results of the potentiodynamic polarisation electrochemical test and ranked the coatings in the same descending order of SB-c > SB-h > WB-c > WB-h regarding protection efficiency.

Ex situ IR RA spectroelectrochemistry showed that the extent of hydration of the coatings was greatest for the hydrophilic WB-h coatings. Analysis of IR RA bands revealed that this coating was characterised by more free C=O groups vs. hydrogen-bonded C=O groups compared to the other investigated coatings. Consequently, the hydrophilic WB-h coating offered the lowest level of protection, which was reflected in the formation of oxides (band at 656 cm^{-1}) at the interface of the coating and the bronze. *In situ* Raman confirmed the

somewhat greater protection afforded by SB-h vs. WB-h coatings. The Raman spectra suggested that Pb diffused from the bronze alloy to the coating and contributed to the formation of lead carbonate with carbonate ions from the electrolyte. The formation of other mixed compounds with chlorides or hydroxides was not excluded.

6. Acknowledgements

This study received funding from the European Union's Horizon 2020 research and innovation programme under grant agreement No. 646063 (NANORESTART, NANOmaterials for the RESToration of works of ART). The Department of Analytical Chemistry, National Institute of Chemistry, is acknowledged for elemental analysis of the bulk bronze substrate. Special thanks to Helena Spreizer for optical measurements. Dr. Cristina Riccucci and Dr. Marianna Pascucci are kindly acknowledged for the SEM and optical analysis.

7. Supporting information

Supporting information may be found in the online version of this article.

8. Data availability statement

The raw/processed data required to reproduce these findings cannot be shared at this time due to technical limitations. On request, they can be sent by the authors.

9. References

[1] L.B. Brostoff, Coating Strategies for the Protection of Outdoor Bronze Art and Ornamentation, Ph.D. Thesis, University of Amsterdam, 2003.

[2] P. Colomban, A. Tournié, M. Maucuer, P. Meynard, On-site Raman and XRF analysis of Japanese/Chinese bronze/brass patina – the search for specific Raman signatures, J.

Raman Spectrosc. 43 (2012) 799–808.

[3] G. Brunoro, A. Frignani, A. Colledan, C. Chiavari, Organic films for protection of copper and bronze against acid rain corrosion, Corros. Sci. 45 (2003) 2219–2231.

[4] G. Bierwagen, T.J. Shedlosky, K. Stanek, Developing and testing a new generation of protective coatings for outdoor bronze sculpture, Prog. Org. Coat. 48 (2003) 289–296.

[5] C. Giuliani, M. Pascucci, C. Riccucci, E. Messina, M. Salzano de Luna, M. Lavorgna, G.M. Ingo, G. Di Carlo, Chitosan-based coatings for corrosion protection of copper-based alloys: A promising more sustainable approach for cultural heritage applications, Prog. Org. Coat. 122 (2018) 138–146.

[6] C. Chiavari, A. Balbo, E. Bernardi, C. Martini, F. Zanotto, I. Vassura, M.C. Bignozzi, C. Monticelli, Organosilane coatings applied on bronze: Influence of UV radiation and thermal cycles on the protectiveness, Prog. Org. Coat. 82 (2015) 91–100.

[7] N.A. Swartz, T.L. Clare, Understanding the differences in film formation mechanisms of two comparable solvent based and water-borne coatings on bronze substrates by electrochemical impedance spectroscopy, Electrochim. Acta 62 (2012) 199–206.

[8] T.J. Shedlosky, A. Huovinen, D. Webster, G. Bierwagen, Development and evaluation of removable protective coatings on bronze, in: Proceedings of Metal 2004, National Museum of Australia Canberra ACT, Canberra, 2004, pp. 400–413.

[9] P. Lo Nostro, L. Scalise, P. Baglioni, Phase separation in binary mixtures containing linear perfluoroalkanes, J. Chem. Eng. Data 50 (2005) 1148–1152.

[10] R.A. Iezzi, S. Gaboury, K. Wood, Acrylic-fluoropolymer mixtures and their use in coatings, Prog. Org. Coat. 40 (2000) 55–60.

[11] R. Parker, K. Blankenship, Fluoroethylene vinyl ether resins for high-performance coatings, in: K.B. Tator (Ed.), ASM Handbook, Protective Organic Coatings, ASM International, 2015, pp. 88–95.

[12] L.R. Krepski, K.M. Lewandowski, D.E. Mickus, S.K. Rowen, S.A. Johnson, Dry-peelable temporary protective coatings, US Patent 6,991,851 B2, 2006.

[13] T. Tysak, Multi-layer coating composition and method of preparation, US Patent 6,855,403 B2, 2005.

[14] V.J. Olson, Keith E., Jackson, Strippable coating system, US Patent 2003/0027010 A1, 2003.

[15] H.G. Edwards, Art works studied using IR and Raman spectroscopy, in: J.C. Lindon, G.E. Tranter, J.L. Holmes (Eds.), Encyclopedia of Spectroscopy and Spectrometry, Academic Press, London, 1999, pp. 2–17.

[16] P. Vandenabeele, H.G.M. Edwards, L. Moens, A decade of Raman spectroscopy in art and archeology, Chem. Rev. (2007) 675–686.

[17] F. Rosi, C. Miliani, C. Clementi, K. Kahrim, F. Presciutti, M. Vagnini, V. Manuali, A. Daveri, L. Cartechini, B.G. Brunetti, A. Sgamellotti, An integrated spectroscopic approach for the non-invasive study of modern art materials and techniques, Appl. Phys. A 100 (2010) 613–624.

[18] P. Letardi, B. Salvadori, M. Galeotti, A. Cagnini, S. Porcinai, A. Santagostino Barbone, A. Sansonetti, An *in situ* multi-analytical approach in the restoration of bronze artefacts, Microchem. J. 125 (2016) 151–158.

[19] G. Di Carlo, C. Giuliani, C. Riccucci, M. Pascucci, E. Messina, G. Fierro, M. Lavorgna, G.M. Ingo, Artificial patina formation onto copper-based alloys: Chloride and sulphate induced corrosion processes, Appl. Surf. Sci. 421 (2017) 120–127.

[20] M. Wadsak, T. Aastrup, I. Odnevall Wallinder, C. Leygraf, M. Schreiner, Multianalytical *in situ* investigation of the initial atmospheric corrosion of bronze, Corros. Sci. 44 (2002) 791–802.

[21] C. Kleber, M. Schreiner, Multianalytical in-situ investigations of the early stages of corrosion of copper, zinc and binary copper/zinc alloys, Corros. Sci. 45 (2003) 2851–2866.

[22] C.M. Johnson, M. Böhmler, Nano-FTIR microscopy and spectroscopy studies of atmospheric corrosion with a spatial resolution of 20 nm, Corros. Sci. 108 (2016) 60–65.

[23] L.B. Brostoff, R. de la Rie, Chemical characterization of metal/coating interfaces from model samples for outdoor bronzes by reflection-absorption infrared spectroscopy (RAIR) and attenuated total reflection spectroscopy (ATR), in: Proceedings of International Congress Metal 98, James & James (Science Publishers) Ltd, 1998, pp. 320–328.

[24] P. Grosse, Conventional and unconventional infrared spectrometry and their quantitative interpretation, Vib. Spectrosc. 1 (1990) 187–198.

[25] B.C. Trasferetti, C.U. Davanzo, M.A. Bica De Moraes, LO-TO Splittings in Plasma-Deposited Siloxane Films, J. Phys. Chem. B 107 (2003) 10699–10708.

[26] I. Jerman, A. Šurca Vuk, M. Koželj, B. Orel, J. Kovač, A structural and corrosion study of triethoxysilyl functionalized POSS coatings on AA 2024 alloy, Langmuir 24 (2008) 5029–5037.

[27] I. Jerman, B. Orel, A. Šurca Vuk, M. Koželj, J. Kovač, A structural and corrosion study

of triethoxysilyl and perfluorooctyl functionalized polyhedral silsesquioxane nanocomposite films on AA 2024 alloy, Thin Solid Films 518 (2010) 2710–2721.

[28] M. Rodošek, A. Rauter, L. Slemenik Perše, D. Merl Kek, A. Šurca Vuk, Vibrational and corrosion properties of poly(dimethylsiloxane)-based protective coatings for AA 2024 modified with nanosized polyhedral oligomeric silsesquioxane, Corros. Sci. 85 (2014) 193–203.

[29] M. Rodošek, A. Kreta, M. Gaberšček, A. Šurca Vuk, *Ex situ* IR reflection-absorption and *in situ* AFM electrochemical characterisation of the 1,2-bis(trimethoxysilyl)ethane-based protective coating on AA 2024 alloy, Corros. Sci. 102 (2016) 186–199.

[30] M. Rodošek, M. Koželj, L. Slemenik Perše, R. Cerc Korošec, M. Gaberšček, A.K. Surca, Protective coatings for AA 2024 based on cyclotetrasiloxane and various alkoxysilanes, Corros. Sci. 126 (2017) 55–68.

[31] C.J. van Oss, R.J. Good, M.K. Chaudhury, Additive and nonadditive surface tension components and the interpretation of contact angles, Langmuir 4 (1988) 884–891.

[32] F. Faraldi, B. Cortese, D. Caschera, G. Di Carlo, C. Riccucci, T. de Caro, G.M. Ingo, Smart conservation methodology for the preservation of copper-based objects against the hazardous corrosion, Thin Solid Films 622 (2017) 130–135.

[33] G.M. Ingo, E. Angelini, T. De Caro, G. Bultrini, I. Calliari, Combined use of GDOES, SEM + EDS, XRD and OM for the microchemical study of the corrosion products on archaeological bronzes, Appl. Phys. A 79 (2004) 199–203.

[34] G.W. Poling, Infrared reflection studies of metal surfaces, J. Colloid Interface Sci. 34 (1970) 365–374.

[35] A. Vilčnik, I. Jerman, A. Šurca Vuk, M. Koželj, B. Orel, B. Tomšič, B. Simončič, J. Kovač, Structural properties and antibacterial effects of hydrophobic and oleophobic sol-gel coatings for cotton fabrics, Langmuir 25 (2009) 5869–5880.

[36] M. Špírková, J. Pavličević, A. Strachota, R. Poreba, O. Bera, L. Kaprálková, J. Baldrian, M. Šlouf, N. Lazić, J. Budinski-Simendić, Novel polycarbonate-based polyurethane elastomers: Composition – property relationship, Eur. Polym. J. 47 (2011) 959–972.

[37] G. Socrates, Infrared and Raman Characteristic Group Frequencies, Tables and Charts, Third Edition, John Wiley, LTD, Chichester, 2009.

[38] L. Xu, C. Li, K.Y.S. Ng, *In situ* monitoring of urethane formation by FTIR and Raman spectroscopy, J. Phys. Chem. A 104 (2000) 3952–3957.

[39] J.C. Hamilton, J.C. Farmer, R.J. Anderson, *In situ* Raman spectroscopy of anodic films

formed on copper and silver in sodium hydroxide solution, J. Electrochem. Soc. 133 (1986) 739–745.

[40] S.T. Mayer, R.H. Muller, An *in situ* Raman spectroscopy study of the anodic oxidation of copper in alkaline media, J. Electrochem. Soc. 139 (1992) 426–434.

[41] S. Härtinger, B. Pettinger, K. Doblhofer, Cathodic formation of a hydroxyde adsorbate on copper (111) electrodes in alkaline electrolyte, J. Electroanal. Chem. 397 (1995) 335–338.

[42] H.Y.H. Chan, C.G. Takoudis, M.J. Weaver, Oxide film formation and oxygen adsorption on copper in aqueous media as probed by surface-enhanced Raman spectroscopy, J. Phys. Chem. B. 103 (1999) 357–365.

[43] B. Willemsen, The Raman spectra of single crystals of $PbCi_2$ and $PbBr_2$ 33 (1971) 3963–3964.

[44] R.L. Frost, W. Martens, J.T. Kloprogge, Z. Ding, Raman spectroscopy of selected lead minerals of environmental significance, Spectrochim. Acta A 59 (2003) 2705–2711.

[45] W.B. White, The carbonate minerals, in: V.C. Farmer (Ed.), The Infrared Spectra of Minerals, Mineralogical Society, London, 1974, pp. 227–284.

Figures and figure captions

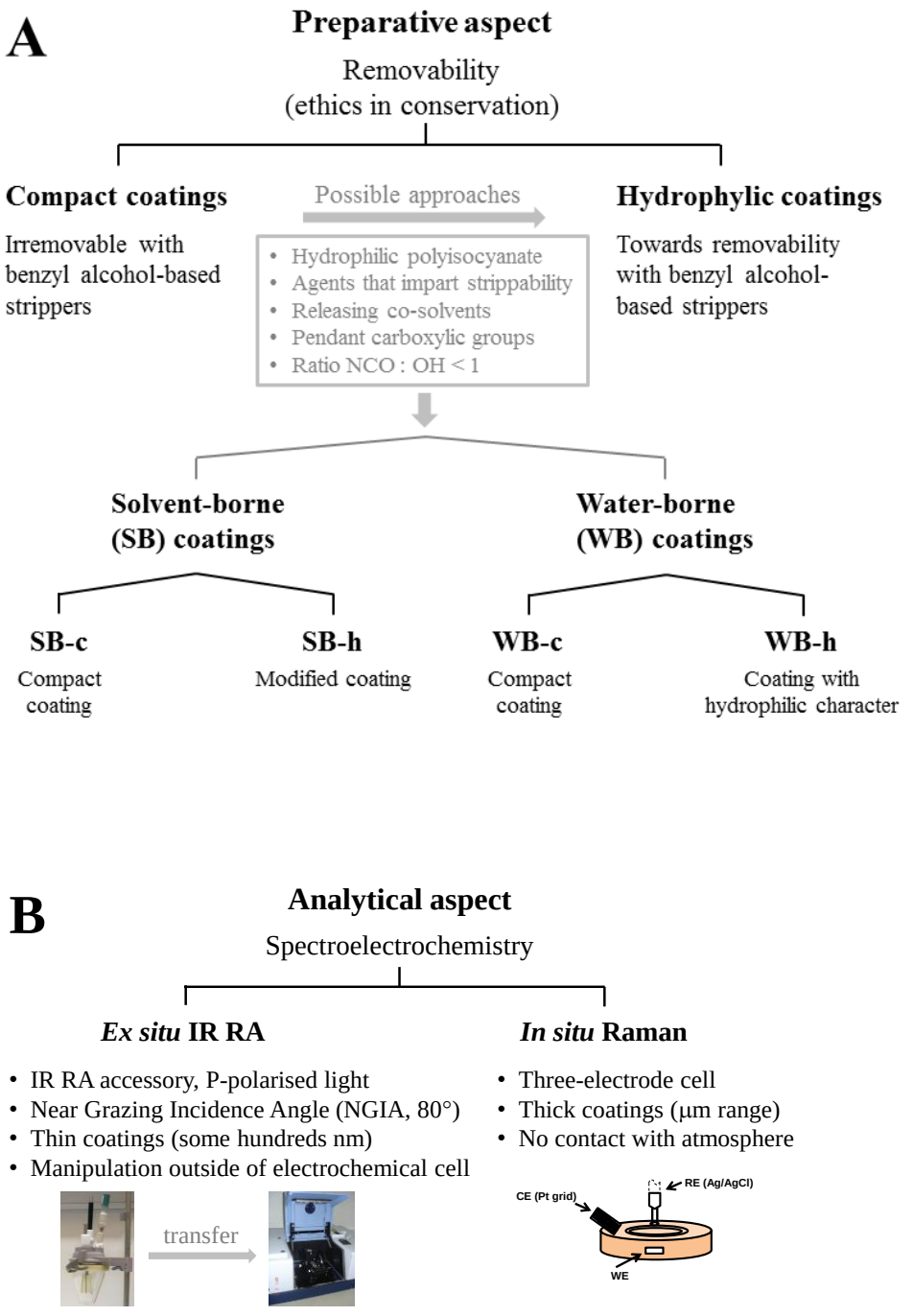

Fig. 1 Schematic representation of the preparative (i) and analytical (ii) aspect of this work.

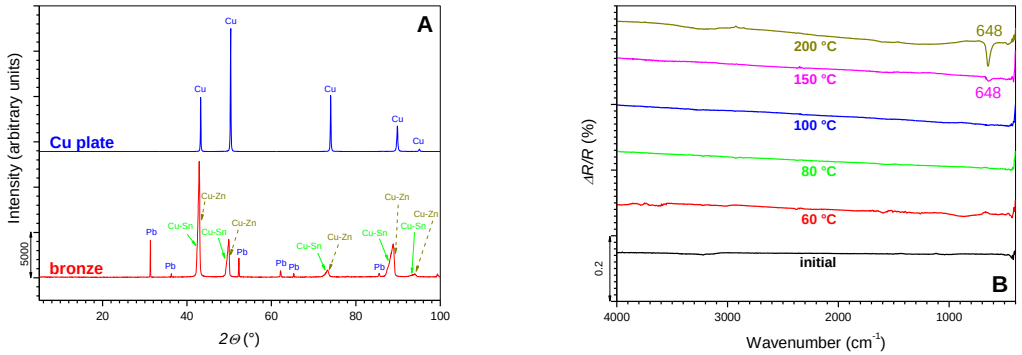

Fig. 2 A) XRD patterns of bronze 85 555 and pure Cu plate and B) IR RA spectra of bronze with successive thermal treatment up to 200 °C (30 min at each temperature). For these measurements, the initial, not thermally treated bronze disk was used as a background.

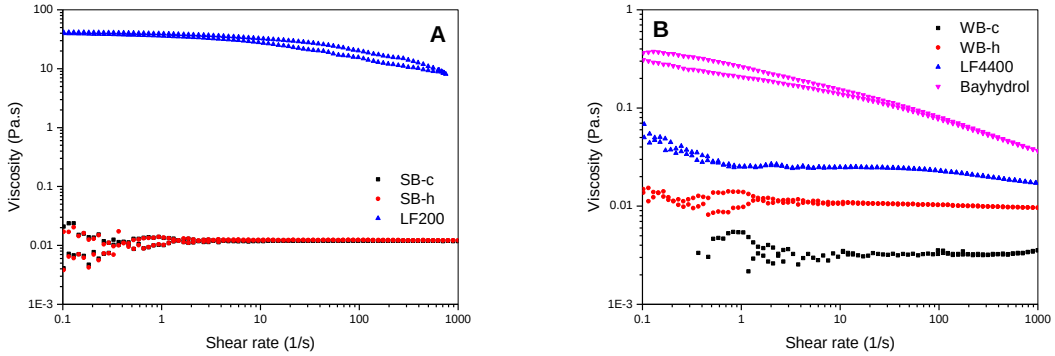

Fig. 3 Flow curves of resins and formulations: A) SB and B) WB.

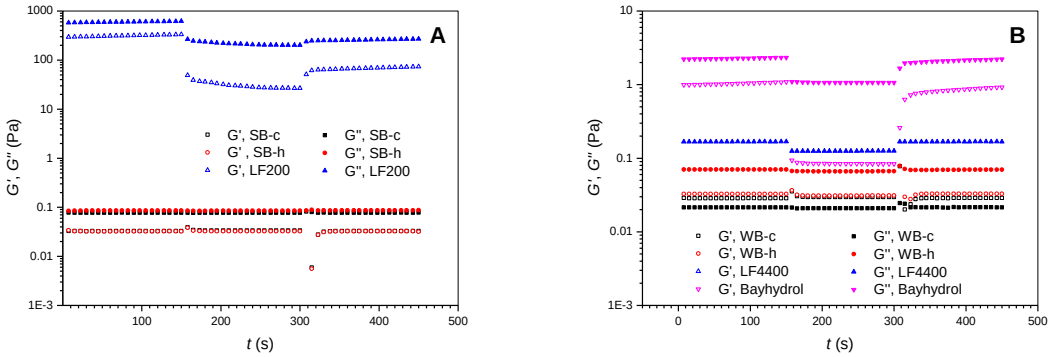

Fig. 4 Three-step time tests for resins and selected A) SB formulations and B) WB formulations.

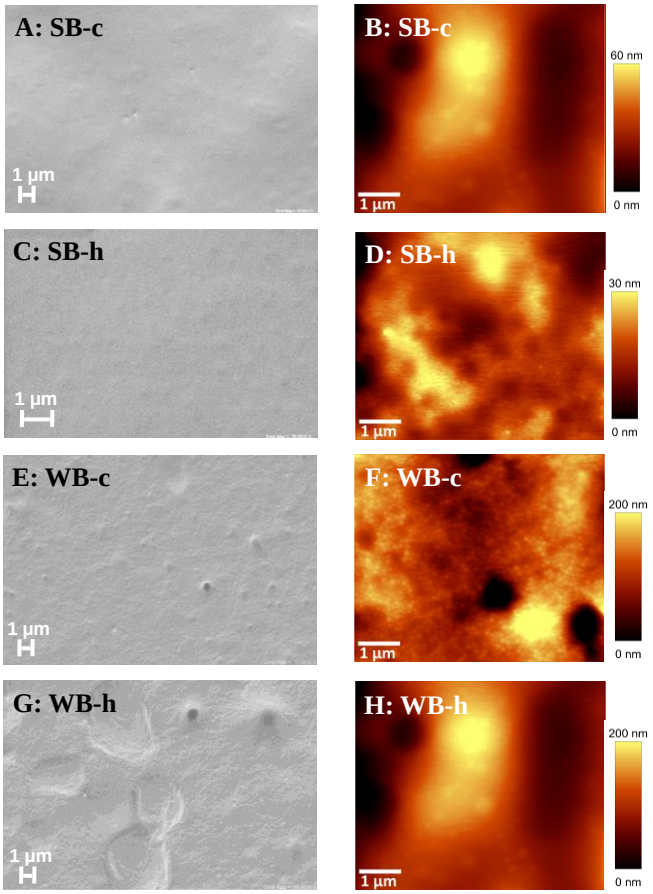

Fig. 5 A, C, E, G) SEM and B, D, F, H) AFM micrographs of protective coatings: A ,B) SB-c, C, D) SB-h, E, F) WB-c and G, H) WB-h. All scale bars are 1 µm.

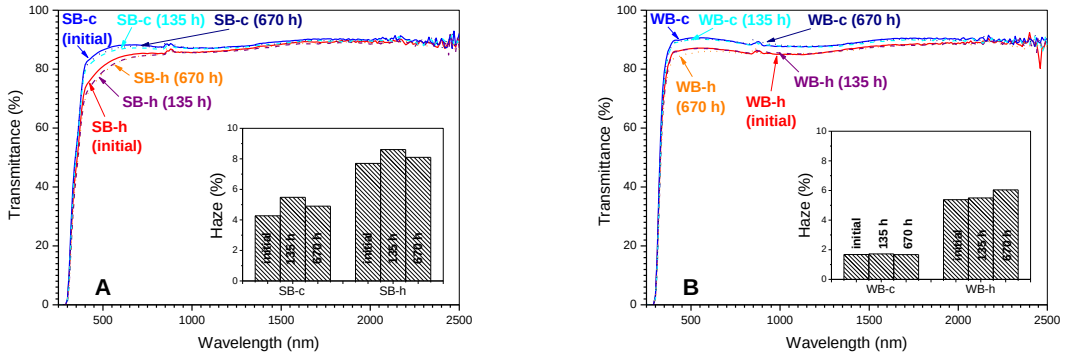

Fig. 6 Transmittance spectra of SB and WB coatings deposited on glass slides - initial spectra and spectra obtained after 135 and 670 h of exposure in Suntest: A) SB-c and SB-h coatings and B) WB-c and WB-h coatings.

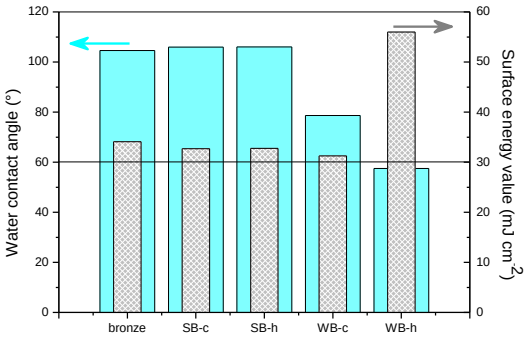

Fig. 7 Contact angles for water (in °) and surface free energy values (in mJ cm^{-2}) of SB and WB protective coatings.

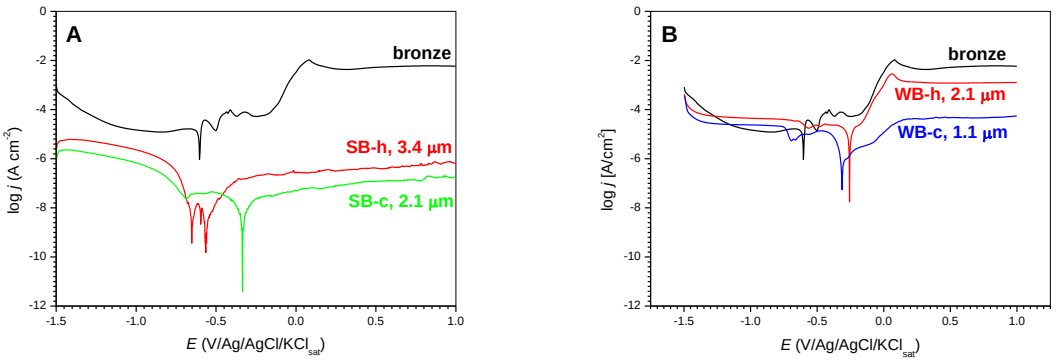

Fig. 8 Potentiodynamic polarisation measurements of: A) SB and B) WB coatings deposited on bronze.

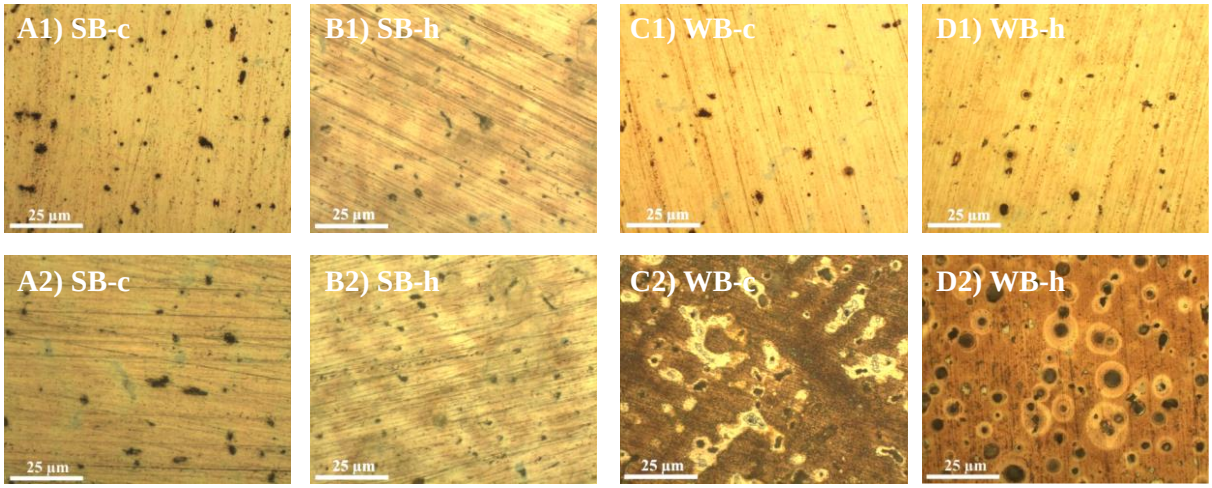

Fig. 9 Optical images of the bronze coated by: A) SB-c, B) SB-h, C) WB-c and D) WB-h passive coatings before (1) and after (2) an accelerated corrosion test for 3 h. The bars on images indicate 25 µm.

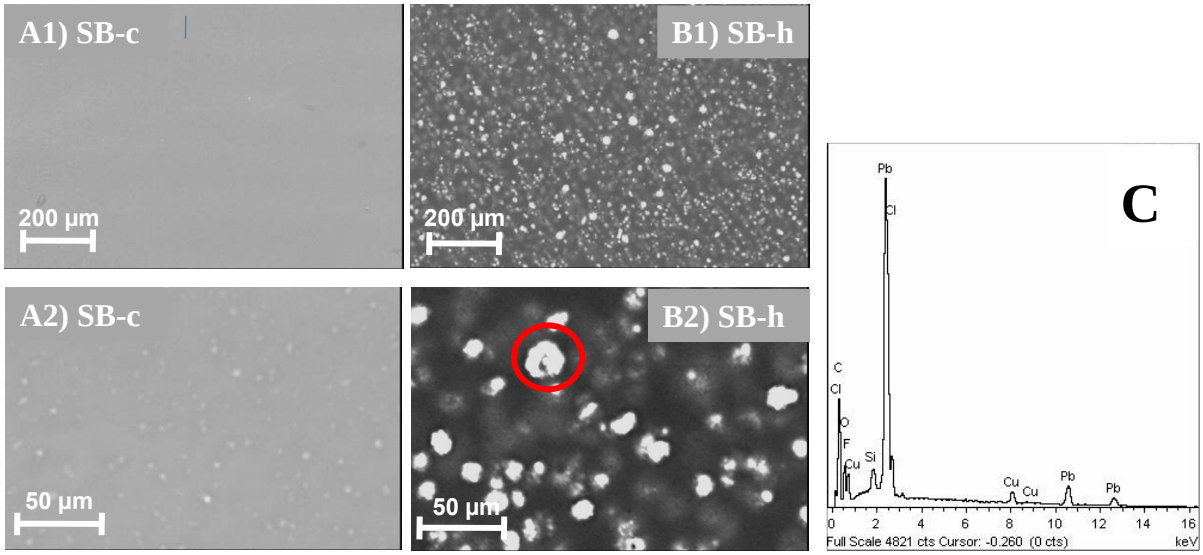

Fig. 10 SEM images of the bronze discs covered by: A) SB-c and B) SB-h coatings. Images in A1 and B1 were recorded before, and images A2 and B2 were recorded after the accelerated corrosion treatment (3 h). C) EDS analysis of the aggregate formed in SB-h coating during the test (marked with a circle).

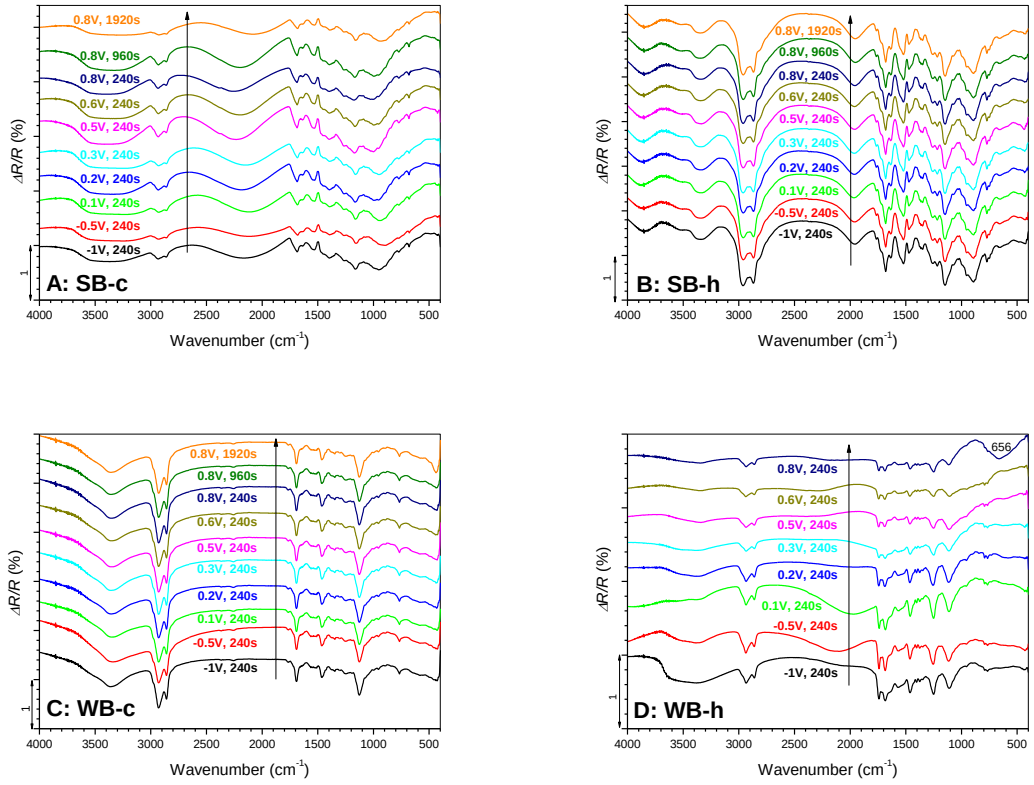

Fig. 11 *Ex situ* IR RA spectra of protective coatings: A) SB-c, B) SB-h, C) WB-c and D) WB-h.

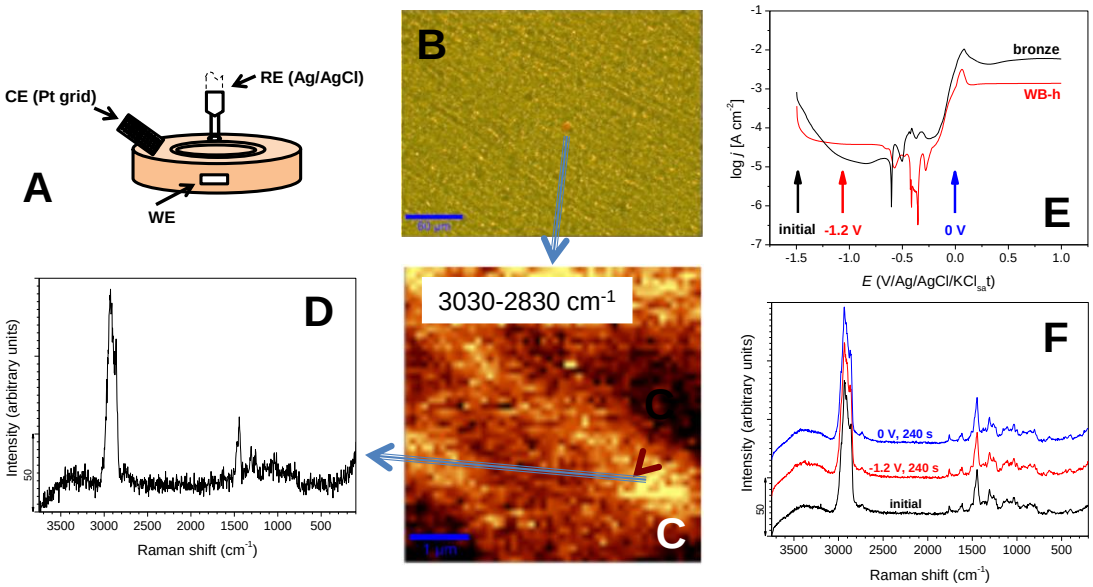

Fig. 12 *In situ* Raman spectroelectrochemical measurements of the WB-h coating: A) *in situ* Raman cell, B) optical image of the initial coating in the electrolyte (scale bar is 60 µm), C) Raman image (scale bar 1 µm) obtained from a 5 × 5 µm^2 square depicted in B), D) Raman spectrum obtained from the bright spot of the Raman image. E) Comparison of the potentiodynamic response of uncovered bronze and bronze covered with WB-h coating. Arrows indicate potentials at which Raman measurements were performed. F) Raman spectra obtained for the initial WB-h coating in the 0.5 M NaCl electrolyte and for the coating treated chronocoulometrically at -1.2 V (240 s) and 0 V (240 s).

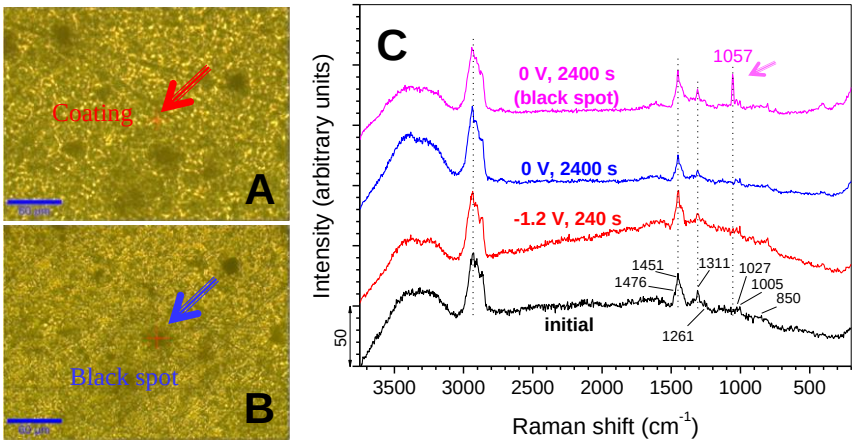

Fig. 13 *In situ* Raman spectroelectrochemical measurements of SB-h coating: A, B) optical images of coating (scale bars are 60 μm) chronocoulometrically treated at 0 V (2400 s). Arrows indicate positions, at which single Raman spectra of coating and black spot were recorded. C) Raman spectra of SB-h coating in the initial state and chronocoulometrically charged to -1.2 V (240 s) and 0 V (2400 s).

Table 1 Compositions of formulations for preparation of SB protective coatings.

	SB-c		SB-h	
Component	**Compound**	**wt.%**	**Compound**	**wt.%**
Resin	LF200	18.2	LF200	16.3
Solvent	butyl acetate	72.7	butyl acetate	65.2
Nano-additive	POSS	1.6	POSS	1.6
Additives	Byk 3441	0.9	2-(2-methoxyethoxy) acetic acid	1.6
			methyl lactate	1.6
			tetraethylene glycol	3.3
Light stabilisers	Tinuvin 1130	0.4	Tinuvin 1130	0.3
	Tinuvin 292	0.2	Tinuvin 292	0.2
Polyisocyanate hardener	Desmodur n75	6.1	Desmodur n75	9.8

POSS – isooctyl-trisilanol-POSS

Table 2 Compositions of formulations for preparation of WB protective coatings.

	WB-c		WB-h	
Component	**Compound**	**wt.%**	**Compound**	**wt.%**
Resin	LF 4400	36.1	LF 4400	18.6
			Bayhydrol UH 340/1	18.6
Solvent	Water	54.1	Water	55.7
Additives			Pluronic F127	3.7
	Byk 028	0.2	Byk 028	0.2
	Byk 349	0.2	Byk 349	0.1
Light stabilisers	Tinuvin 5333-DW	1.4	Tinuvin 5333-DW	1.5
Polyisocyanate hardener	Easaqua XD 401	8.0	Bayhydur XP 2655	3.2

Table 3 Concentration of Sn, Zn and Pb in bronze 85 555 as determined by EDS at different positions (spectra 1 to 3) vs. actual bulk concentration.

Measurement	**Cu**	**Sn**	**Zn**	**Pb**	**C**
Spectrum 1	87.4	6.3	4.2	2.1	/
Spectrum 2	70.9	6.2	2.4	17.1	3.4
Spectrum 3	19.9	2.4	/	63.9	6.7
Bulk	rest	4.5	5.3	5.2	

All concentrations in wt.%.

Table 4 IR band frequencies of SB and WB coatings.

IR band	Type of vibration
2929 – 2962 2875 – 2860	CH_2 stretching, asymmetric and symmetric
1765 – 1741	free C=O
1726 – 1717 1691 – 1682 1637 – 1635	differently hydrogen-bonded C=O groups
1470 – 1440	CH_2 bending
1111 – 1163	CF_2 from resins; C-O from resins

Table 5 Raman band frequencies of SB and WB coatings.

IR band	Type of vibration
~3300	OH groups from electrolyte
2950 – 2850	CH_2 stretching, asymmetric and symmetric
1760	-NH-CO-O- bond
1476 sh 1451 s	$\delta(CH_2)$ NCO
1307 – 1311	$\delta(CH_2)$ wagging;
1261	$\delta(CH_2)$ twisting
1235	ν(C-N), ν(C-O)
1027	ν(C-F)